Cr/GLC multilayered coating in simulated deep-sea environment: Corrosion behavior and growth defect evolution

Yingrui Liu [a,b], Hong Du [c], Xiao Zuo [a], Peng Guo [a], Li Liu [d], Kwang-Ryeol Lee [e], Aiying Wang [a,b,*], Peiling Ke [a,b,*]

[a] *Key Laboratory of Marine Materials and Related Technologies, Zhejiang Key Laboratory of Marine Materials and Protective Technologies, Ningbo Institute of Materials Technology and Engineering, Chinese Academy of Sciences, Ningbo, 315201, PR China*
[b] *Center of Materials Science and Optoelectronics Engineering, University of Chinese Academy of Sciences, Beijing, 100049, PR China*
[c] *Nano Science and Technology Institute, University of Science and Technology of China, 215123, Suzhou, PR China*
[d] *Shenyang National Laboratory for Materials Science, Northeastern University, Shenyang, 110819, PR China*
[e] *Computational Science Center, Korea Institute of Science and Technology, Seoul, 136-791, Republic of Korea*

ARTICLE INFO

ABSTRACT

In this work, the corrosion behavior of the multilayered Cr/GLC coating was evaluated in artificial seawater by comparison at an atmospheric pressure (1 atm) and a higher hydrostatic pressure (300 atm). The results revealed that the corrosion resistance of the coating was more favorable at 1 atm, but the hydrostatic pressure deteriorated coating protectiveness significantly by rapidly accelerating seawater diffusion through the growth defect and promoting the exposure of the substrate. The localized corrosion induced by the penetrating defect became more susceptible. This study is helpful to bring forward the significant guideline to fabricate the dense coating for deep-sea applications.

1. Introduction

In recent years, more and more efforts have been devoted to the deep-sea resource exploitation as it plays important roles in the sustainable development of human society. But the effective exploration of deep-sea resources is challenged by the unique and special conditions, such as hydrostatic pressure, different concentrations of dissolved oxygen, salts solution, suspended silt, and water velocity etc. [1]. Especially, the hydrostatic pressure increases monotonically with the ocean depth, playing a critical role in the change of the corrosion reaction. It can even accelerate the corrosion process of the facilities operating in the deep-sea environment [2].

Lots of researchers have investigated the effect of the hydrostatic pressure on the corrosion behavior of the metals/alloys in laboratory experiments. In the earlier stage, Beccaria et al. studied the corrosion behavior of several alloys as a function of simulated hydrostatic pressure in sea water environment [3,4]. They pointed out the hydrostatic pressure enhanced the susceptibility to pitting corrosion of the pure aluminum owing to the promoted breakdown of the oxidation layer [5]. But the pitting susceptibility to the 6061 T6 aluminum alloy have been

affected little due to the formation of the more protective Mg-Al oxide layer [6]. The corrosion behavior of some low alloy steels and passive alloys applied in deep-sea, such as X70 steel [7], Ni-Cr-Mo-V high strength steel [8] and Fe-20Cr alloy [9], were also studied. It has been proved that the hydrostatic pressure deteriorated the corrosion resistance in the aspect of increased pitting generation rate. Obviously, the bare metals/alloys easily suffer from an accelerated corrosion process in deep-sea environment.

Surface protective coating technologies are highly effectual method to avoid the premature corrosion failure of the components in deep-sea. Organic coatings can strictly restrict the transport of corrosive media to bare metal/alloy substrate and result in a long-term appreciable protection, which is one kind of the most widely studied protective coating materials in deep-sea [10–13]. The sprayed amorphous coating with high strength and appropriate corrosion resistance is another candidate coating material for the harsh deep-sea environment [14]. However, neither of them has comprehensive properties with the corrosion resistance and the mechanical performance. When the service conditions of the components involve severe frictions and corrosions in deep-sea environment, such as plungers in water hydraulic pumps, water

lubricated bearings and other friction pairs, the development of novel protective coatings with superior tribocorrosion resistance are highly desirable [15].

The graphite-like carbon (GLC) coating, with predominate sp^2-hybridized carbon, has the comprehensive performances like high hardness, low friction coefficient and good chemical inertness. These features endow the GLC coating with excellent corrosion resistance in water lubrication conditions and make it considered to be an ideal candidate of the protective coating in deep-sea environment [16]. The corrosion behavior or the failure mechanism of the GLC coating in corrosive environment has been carried out under atmospheric pressure environment. Manhabosco et al. [17] found that GLC films deposited on the bare and nitride titanium alloy both presented significantly high corrosion resistance at the initial time, but the film deposited on the nitride alloy showed delamination and cracks after 16-day immersion tests, which was interpreted as the existence of pores combined with the weak film/substrate adhesion. Yan et al. [18] reported that the Cr-GLC nanocomposite film improved the corrosion resistance of the substrate with two orders of magnitude due to the chemical inertness of Cr-GLC nanocomposite films. Noted that although the GLC coatings are usually electrochemical nobler than the substrates, they inevitably contain some growth defects during deposition process. Growth defects provide the channels for the transportation of corrosive species (e.g. Cl^- and O_2) and corrosion products, resulting in a sustainable corrosion reaction in the deep-sea environment. Even worse, the interface electrochemical reaction would occur through the growth defects and the adhesion strength would be deteriorated simultaneously, which are unacceptable for the long-term application [19,20]. Therefore, the compactness of GLC is critical for the corrosion resistance.

Recently, the multilayered structure design [21]with buffer layer [22] and atomic layer deposition (ALD) technology [23] were adopted to heal the growth defects and optimize the performance of the a-C coating. In comparison, the multilayered structure design is a fundamental approach to improve the integrated performance. Some investigations conducted at atmospheric pressure environment demonstrated that the proper modulation ratio and optimized multilayer structure could significantly improve the corrosion resistance by prolonging the diffusion path of corrosive species through the growth defects [24,25]. While the complex interface structure induced by the multilayered design may cause other problems such as galvanic corrosion [26]. Therefore, it is worthwhile to study the corrosion behavior, especially the interface corrosion reaction of the multilayered GLC coating in deep-sea environment. However, the research on the corrosion behavior of GLC coatings in deep-sea environment hasn't been undertaken yet.

In this work, the multilayered Cr/GLC coatings were fabricated with the hybrid magnetron sputtering technique. The effect of the hydrostatic pressure on the corrosion behavior of the coating was focused. Meanwhile the corrosion mechanism of the Cr/GLC multilayered coating was comprehensively discussed in terms of growth defects and the microstructural evolution during electrochemical tests. The most significant meaning of this study is that this is the first investigation of the dependence of corrosion behavior upon the hydrostatic pressure for Cr/GLC multilayered coating, which is not only helpful to understand the corrosion mechanism of multilayered structure coating, but also provides a helpful guideline for the development of excellent anti-corrosion performance GLC coating applied in the deep-sea environment.

2. Experimental details

2.1. Coating preparation and characteristics

The Cr/GLC multilayered coatings were deposited on P-type (100) Si wafers and the polished 316 L stainless steels (18 mm × 18 mm×3 mm) by an alternative deposition method. The coating deposition equipment was configured with a pure chromium target (99.9 %), a pure graphite

target (99.99 %) in size of 400 mm × 100 mm×5 mm, and a linear ion source (LIS), as shown in Fig.S1 (Supporting Information). Prior to deposition, the substrates were cleaned in acetone, ethanol in sequence and dried with a dryer. The distance from the substrate to the target was 10 cm. The chamber vacuum was exhausted to a value of about 2.0×10^{-5} Torr, and then all the substrates were etched and precleaned with Ar + ion source for 40 min with a negative bias of −100 V.

The deposition process contains the modulated pulsed power magnetron sputtering (MPPMS) technique and the direct current magnetron sputtering (DCMS) technique. Cr/GLC coating with certain modulation periods was obtained by commutative deposition of MPPMS-Cr layers and DCMS-GLC layers. During coating deposition, the Argon flow rate was kept at 55 sccm. The multilayered structure deposition processed as follows. First, a combination of (Cr + Cr_xN) layer using MPPMS was deposited and set as the buffer layer to enhance the interfacial bond strength, while the rest of the buffer layers was deposited with pure Cr only. The Cr buffer layer was deposited on the substrate with a target current of 1.2A and a bias voltage of −100 V. The deposition of Cr_xN layer adopts a nitrogen (N_2) flow of 15 sccm. Afterwards, the graphite target was used to deposit the GLC layers by DCMS with a target current 3.0 A and a bias voltage of −200 V. The deposition procedures of Cr and GLC coating were set as one block. The block was repeated 8 times to form Cr/GLC multilayered coating. The schematic diagrams of the Cr/GLC multilayered coating shown in Fig. 1.

2.2. Simulation of deep-sea environment

The in-situ electrochemical tests and immersion tests under both hydrostatic pressures were carried out by using the autoclave corrosion test system (CORTEST Inc. USA), which was equipped with a plunger pump, temperature control system, monitoring system and electrochemical work station. The schematic graph of the autoclave corrosion test system was illustrated in Fig. S2. The artificial seawater was prepared according to the standard of artificial seawater [27], as shown in Table 1. To simulate the deep-sea environment correctly, the dissolved oxygen concentration, pH value and temperature of the artificial seawater were controlled in proper value correspondingly [28]. In the present study, a high hydrostatic pressure (300 atm) and a low temperature (6 ℃) were set to simulate the 3000 m depth deep-sea environment. As a contrast, an atmospheric pressure (1 atm) and a temperature of 25 ℃ were equaled to the shallow sea environment. The pH value of artificial seawater was controlled at 7.48. Before the electrochemical tests the pure nitrogen gas was pumped into the artificial seawater to control the dissolved oxygen concentration at an appropriate level (about 4.96 mL/L), which was corresponded to the simulated deep-sea environment (300 atm, 6 ℃).

2.3. In-situ electrochemical and immersion tests

Before electrochemical tests, the coating specimens were connected to a copper cable and embedded in epoxy resin. The exposed area of the Cr/GLC multilayered coating was 0.64 cm^2. All the electrochemical experiments were performed on Reference 600+ (Gamry, USA) electrochemical workstation equipped with a three-electrode cell configuration. The Cr/GLC multilayered coating was set as the working electrode and the platinum plate as the counter electrode. A high pressure-resistant Ag/AgCl solid electrode was chosen as the reference electrode under both hydrostatic pressure environments.

Various electrochemical tests were carried at 300 atm and 1 atm in the artificial seawater to investigate the effect of the hydrostatic pressure on the corrosion resistance of the Cr/GLC multilayered coating. The cyclic polarization tests with a scanning rate of 0.2 mV s^{-1} from −0.4 V below the corrosion potential (E_{corr}) to the anodic direction. The apex current density of the cyclic polarization tests was set as 0.02 mA cm^{-2}, and the potential was reversed with the same scanning rate once the corrosion current density reaching the apex value. The breakdown
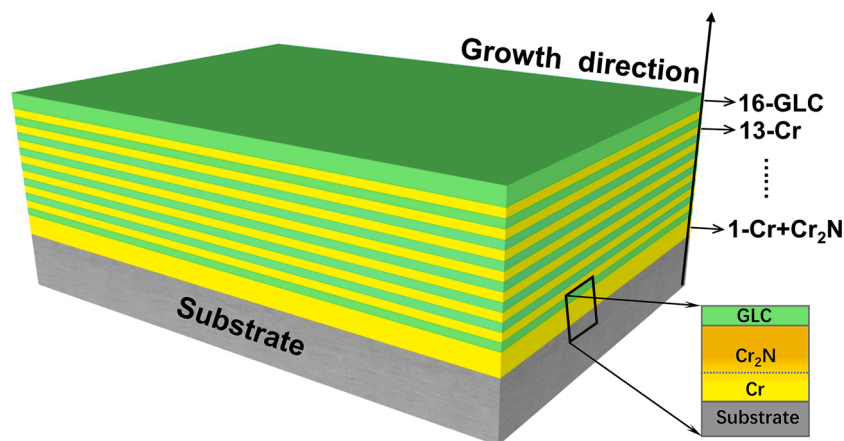
Fig. 1. The schematic view of the Cr/GLC multilayered coating.

Table 1
Chemical Composition of Artificial Seawater(g/L).

Constituent	NaCl	MgCl$_2$	Na$_2$SO$_4$	CaCl$_2$	KCl	NaHCO$_3$	KBr	HBO$_3$	SrCl$_2$	NaF
Concentration	24.53	5.20	4.09	1.16	0.695	0.201	0.101	0.027	0.025	0.003

potential (E$_b$) was determined when the corrosion current density reached 0.01 mA cm^{-2} and the protection potential (E$_{prot}$) was determined when the backward scan was intersected with the forward scan. The difference (η_{pp}) between the E$_b$ and E$_{prot}$ was defined as the measurement to evaluate the anti-localized corrosion. To stabilize the surface of coatings, all the cyclic polarization tests were performed by using an initial delay time at the equilibrium state for 1 h. In-situ EIS tests during the immersion test were performed to record the change of corrosion resistance under both hydrostatic pressures. The EIS tests were conducted with perturbing AC amplitude of 10 mV at the scanning frequency ranged from 10^5 Hz to 10^{-2} Hz. All the tests' data were analyzed and fitted with the electrical equivalent circuit models with the ZSimpwin software. After the immersion tests, the potentiostatic polarization test conducted under the constant potential of 600 mV$_{Ag/AgCl}$ above the E$_{corr}$ for 1 h was carried out.

2.4. Characterization of the Cr/GLC multilayered coating

Surface morphologies of the Cr/GLC multilayered coating were observed using a scanning electron microscope (SEM, FEI Quanta FEG 250)) equipped with an energy dispersive spectrometer (EDS). Transmission electron microscopy (TEM, Talos F200x) observation in the high-angle annular-dark-field (HADDF) mode was performed to investigate the cross-sectional microstructure of the Cr/GLC multilayered coating. The surface growth defects morphologies, before and after immersed tests, were studied in a planar surface view and cross-sectional view by using focus ion beam (FIB, Carl Zeiss Auriga) technique. Surface chemical compositions were characterized by the X-ray spectroscopy (XPS, Thermo Scientific ESCALAB 250). Prior to XPS tests, the Cr/GLC multilayered coatings' surface was cleaned by Ar + etch with 1 min. The C1 s peak (284.6 eV) was used to correct the binding energies of electrons.

3. Results

3.1. Morphology and microstructure of the as-deposited coating

Fig. 2 shows the surface morphology and typical growth defects of the as-deposited coating. Although the coating surface seems smooth at low magnification (Fig. 2(a)), the inserted high-resolution image presents the undulating microstructure with lots of nanopores. Moreover, several typical growth defects can be easily observed from the surface. The corresponding enlarged draws combined with the EDS mapping contrast from A and B positions have shown in Fig. 2(b–c), respectively. Fig. 2(b) clearly indicates that this kind of defect belongs to the open-type and is filled with a very thin coating on the bottom of the defect.
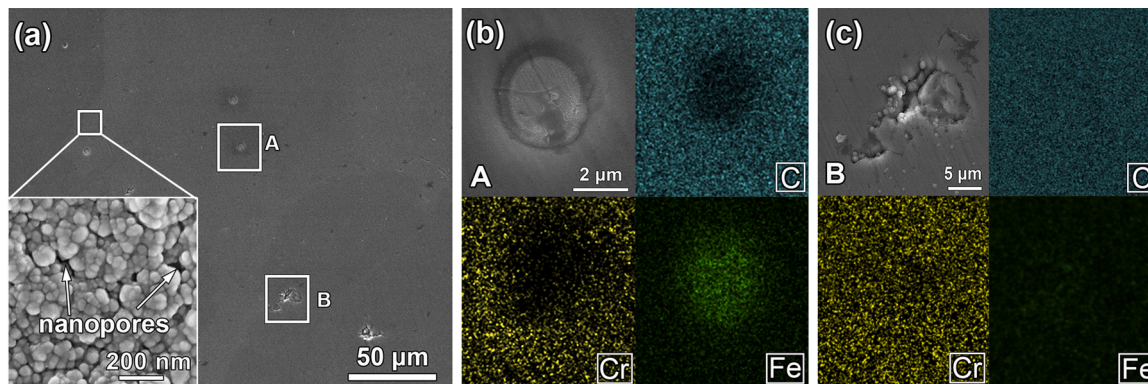

Fig. 2. Surface morphology of the as-deposited coating(a), detail image of penetrating defect (b) and nodular-like defect (c) and their corresponding EDS mapping results.

Another kind of defect exhibits the characteristics with partial deletion of coating and some globular particles distributes surrounded (Fig. 2(c)). EDS results do not provide the image of substrate directly. Based on these features, the two types growth defects are classified as the penetrating defect and nodular-like defect.

The cross-sectional TEM microstructure of the as-deposited Cr/GLC multilayered coating is shown in Fig. 3. Notably, the coating displays a periodic multilayered structure and the thickness is about 1 μm (Fig. 3 (a)). Due to the coarse columnar grains formed on the first buffer layer (Fig. 3(b)), the following layers deposited on it alternatively presents a wave feature. The first buffer layer's SAED pattern exhibits typical nanocrystalline characteristics of the Cr_2N phases. Some inter-and intra-columnar pores are visible in the high-magnification image of Fig. 3(d), but the GLC layers deposited on the Cr buffer layer are much denser and still present the amorphous nature. The characteristics of this multi-layered coating indicate that the microdefects (pin-pores) existed in the single Cr layer can be healed by the alternative deposition of GLC layers.

3.2. Electrochemical corrosion results

3.2.1. In-situ EIS results obtained from immersion tests

All the in-situ EIS results, which was conducted during 240 h immersion both at 1 atm and 300 atm, are displayed as Nyquist plots and Bode plots in Figs. 4 and 5, respectively. The EIS results collected under both two environments prove that the corrosion resistance of the coatings changed with increasing hydrostatic pressure. At the atmospheric pressure, four moments were collected to evaluate the variation of corrosion resistance at three stages: prophase (0.5 h and 2 h), metaphase (120 h) and anaphase (240 h). The EIS plots obtained at 1 atm reveal that the immersion test almost has little impacts on the corrosion resistance of coatings. During the whole immersion test, there is one capacitive loop and the phase angle remains high values (>80°) in a large frequency range (10^{-2} Hz–10 Hz). This suggests that the Cr/GLC multilayered coating could maintain a stable corrosion protective performance under atmospheric pressure.

By contrast, the high hydrostatic pressure has a more significant impact on the corrosion resistance of the coating during the immersion test. The Nyquist plot (Fig. 5(a)) presents a gradual decline characteristic of capacitive loops at the entire immersion period. The Bode plots (Fig. 5(b)–(d) also show the significant change of phase and impendence modules during the immersion. According to the number of time

constant exist at phase Bode-degree plot, the influence of hydrostatic pressure on the corrosion resistance of the coating during immersion can be divided into different stages. The impendence data at the initial stage (0.5 h–2 h) reveal two time constants, which is similar with the results under atmospheric pressure. After 2 h, the first time constant at high frequency ($\sim 10^3$ Hz) indicates a lower phase angle, reflecting a deteriorated coating protection performance. After about 9 h, phase angle at high frequency does not change with immersion time, but decrease obviously at low frequency ($\sim 10^{-2}$ Hz).

From these EIS results, it can be deduced that the hydrostatic pressure deteriorates the protection performance of the coating, and meanwhile the corrosion behavior of the Cr/GLC multilayered coating is also changed.

3.2.2. Cyclic polarization tests and corrosion morphologies

Fig. 6 shows cyclic polarization curves and corresponding corroded morphologies of the Cr/GLC multilayered coating under both environments after immersion 1 h. Obviously, the hydrostatic pressure has a significant influence on the localized corrosion behavior of the coating. The electrochemical parameters obtained from cyclic polarization curves are listed in Table 2. The E_{corr} shifts negatively about 91.5 mV with the increasing hydrostatic pressure from 1 atm to 300 atm, which indicates that the coating is more susceptible to corrosion under higher hydrostatic pressure condition. The curve of the coating at 1 atm shows a not distinct hysteresis loop, but it displays a significant hysteresis loop at 300 atm. The appearance of current hysteresis loop proves that the hydrostatic pressure promotes the localized corrosion reaction and a delayed repassivation process. The larger the integral area of the hysteresis loop is, the more difficult it becomes to repassivate the localized corrosion [29].

Typical corrosion morphologies after cyclic polarization tests are shown in Fig. 6(b) and (c). The difference in the number and the size of the corrosive site is remarkable. Some nodal-like defects and tiny penetrating defects can be observed from the morphology at 1 atm (Fig. 6(b)), which is similar with the as-deposited coating. This indistinct change of coating surface features implies the slight corrosion reaction, which is consistent with its complete disappeared breakdown phenomenon. However, more large-sized corrosion pits appear in the coating (Fig. 6(c)) after the polarization test at 300 atm, indicating the more seriously localized corrosion. Above-mentioned results manifest that the hydrostatic pressure results in a deteriorated localized corrosion
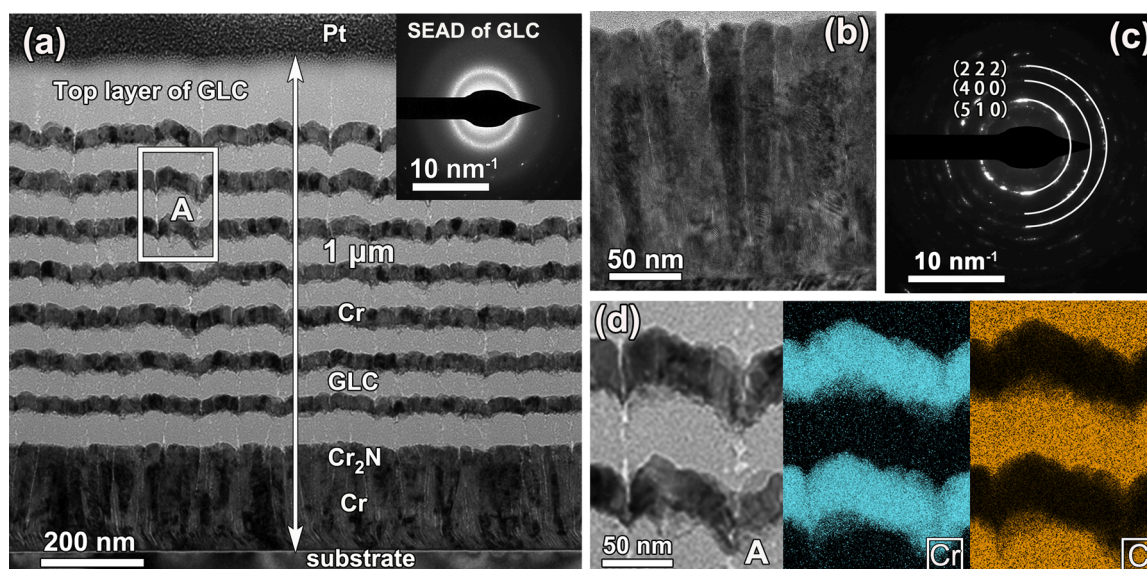

Fig. 3. The cross-sectional TEM bright-field images taken (a) from the as-deposited Cr/GLC multilayered coating (a). (b) HRTEM image at the bottom buffer layer of Cr + Cr_2N and (c) is the corresponding SAED patterns. The enlarged draw taken from the marked A position and its corresponding EDS mapping results.
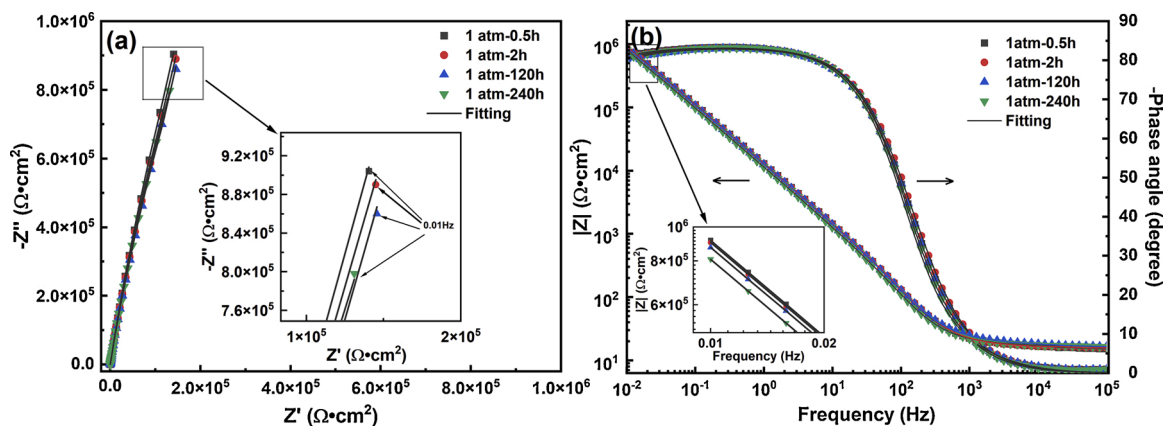
Fig. 4. The in-situ EIS results with immersion time under atmospheric pressure (1 atm), (a) the Nyquist plots of coating, (b) Bode plots of coating. The scatter points in this figure are the measured data points, and the black line is the fitting results according to the equivalent circuit models.
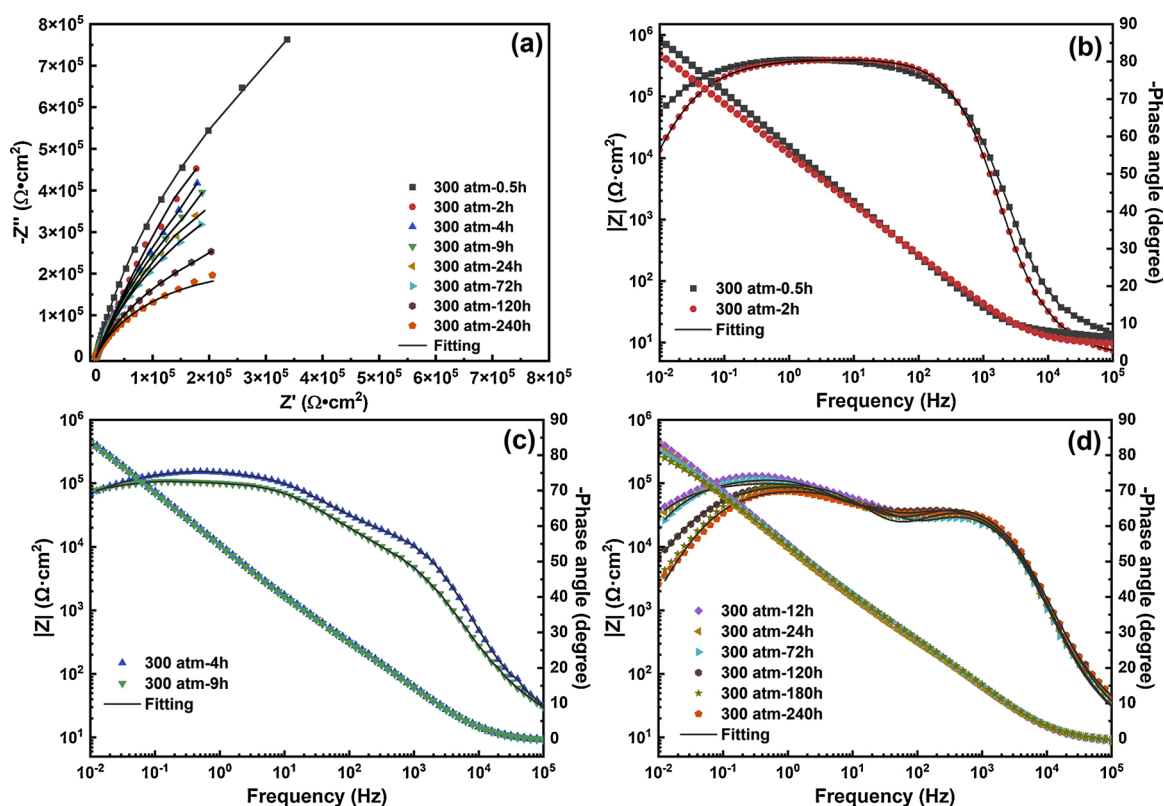

Fig. 5. The in-situ EIS results with immersion time under high hydrostatic pressure (300 atm), (a) is Nyquist plots of coating during the whole immersion test, (b)-(d) the Bode plots of coating at different immersion time. The scatter points in this figure are the measured data points, and the black line is the fitting results according to the equivalent circuit models.

protection performance of the Cr/GLC multilayered coating.

3.2.3. Potentiostatic polarization tests

Potentiostatic polarization tests were carried out at constant potential to evaluate the localized corrosion initiation under both environments. Fig. 7(a) shows quite different features both on the number of current transient peaks and the stable current density. The curve obtained at 1 atm shows a fairly smooth feature and extremely low current density about $2.536 \times 10^{-7}\,\mathrm{A\,cm^{-2}}$. However, the curve obtained at 300 atm exhibits specific metastable localized corrosion and increased current density of $2.109 \times 10^{-6}\,\mathrm{A\,cm^{-2}}$. Furthermore, in order to clarify the origin of the current transients, the characteristic of metastable current transients appeared at higher hydrostatic pressure are analyzed in Fig. 7

(b). Pit growth time (t1), repassivation time (t2) and life time (t3) are used to character the current transient. It can be found from the shape of enlarged current transient that the current first exhibits a gradual rise (t1≈2 s) but then quickly current drop (t2≈1 s). The lift time (t3) of the current transient is about 3 s, which reveals an agreement with the pitting corrosion characteristics of the stainless steel substrate [30]. Consequently, it can be deuced that the current transient at 300 atm originates from the dissolution of substates. The rise of current is mostly due to the breakdown of the passive film on the exposed substrate at the bottom of penetrating defects, while the quickly decay is corresponding to the reformed passive film. The occurrence of transient peaks as well as the relative higher current density at 300 atm indicates that the seawater has reached to the bottom of the penetrating defects and the substrate
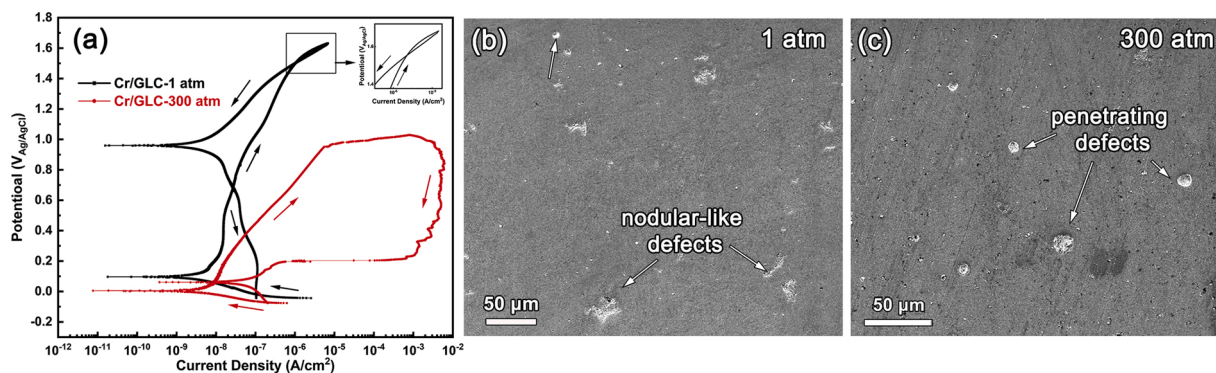
Fig. 6. Cyclic potentiodynamic polarization curves obtained from the Cr/GLC multilayered coating under both hydrostatic pressures (a) and its corresponding corrosion morphologies(b-c) after the tests.

Table 2
The electrochemical parameters of the cyclic polarization tests for Cr/GLC multilayered coating under both hydrostatic pressures.

Hydrostatic pressure (atm)	E_{corr} (mV$_{Ag/AgCl}$)	E_b (mV $_{Ag/AgCl}$)	E_{prot} (mV $_{Ag/AgCl}$)	η_{pp}(mV)
1	96.3		1507.2	\
300	1.2	979.5	62.7	1444.5

corrosion reaction has accrued.

3.3. XPS analysis

The XPS tests were conducted to provide the chemical composition information on the Cr/GLC multilayered coating surface after 240 h immersion under both environments. Fig. 8 shows the detailed XPS spectra of O 1s, C 1s, Cr 2p$_{3/2}$ and Fe 2p$_{3/2}$. The response peaks of O 1s are fitted with three components for t O^{2-}, OH$^-$ and H$_2$O both under two environments, respectively, but the concentration of the three components is totally different. The low- bonding energy response peaks of O^{2-} and OH- are attributed to the metal oxide and oxygen-deficient regions (i.e., O vacancies) [31]. The high-bonding energy peak (H$_2$O) is assigned to the near-surface oxygen and the chemical adsorbed oxygen (i.e., O$^-$ and OH$^-$) [32]. After 240 h immersion at 300 atm, the appearance of the H$_2$O peak indicates that the domain O species on the coating surface clearly change from both O^{2-} and OH$^-$ to H$_2$O and OH$^-$.

Fig. 8(b) presents the response peaks of C 1s. The C 1s peak at 1 atm is only deconvoluted to three peaks corresponding to the sp^2 carbon (C = C), sp^3 carbon (C-C) and C = O, respectively [33]. Differently, new peaks appear at 287.02 eV (C-Cl) and 288.8 eV (CO$_3^{2-}$). Therefore, it indicates that the hydrostatic pressure enhances the absorption of Cl- in the artificial seawater environment.

XPS spectra of Fe 2p$_{3/2}$ are presented in the Fig. 8(c). The response peaks are fitted with three peaks for the Fe, Fe$_2$O$_3$ and FeOOH, respectively. No any other peak presents at 300 atm, but the proration of the Fe$_2$O$_3$ and FeOOH increased slightly. Compared with the other element, the Cr 2p$_{3/2}$ spectra (shown in Fig. 8(d)) does not shows specie peaks clearly. The envelope line of the Cr 2p$_{3/2}$ shows an obvious jumping characteristic compared with the O 1s and C 1s. According to the XPS analysis of the different element after immersion at 300 atm, the surface of the coating mainly contains Fe$_2$O$_3$, FeOOH and lots of adsorbed H$_2$O, indicating that the corrosion reaction mainly occurred on the substrate and the corrosion products can diffuse from the bottom of penetrating defect to the coating surface.

4. Discussion

According to the above-mentioned results and considering of the amorphous carbon coating being inert enough in the artificial seawater, it can be deduced that the electrochemical dissolution reaction primarily takes place at the imperfects of those exposed substrate sites [16,17]. The surface morphology of the as-deposited Cr/GLC multilayered
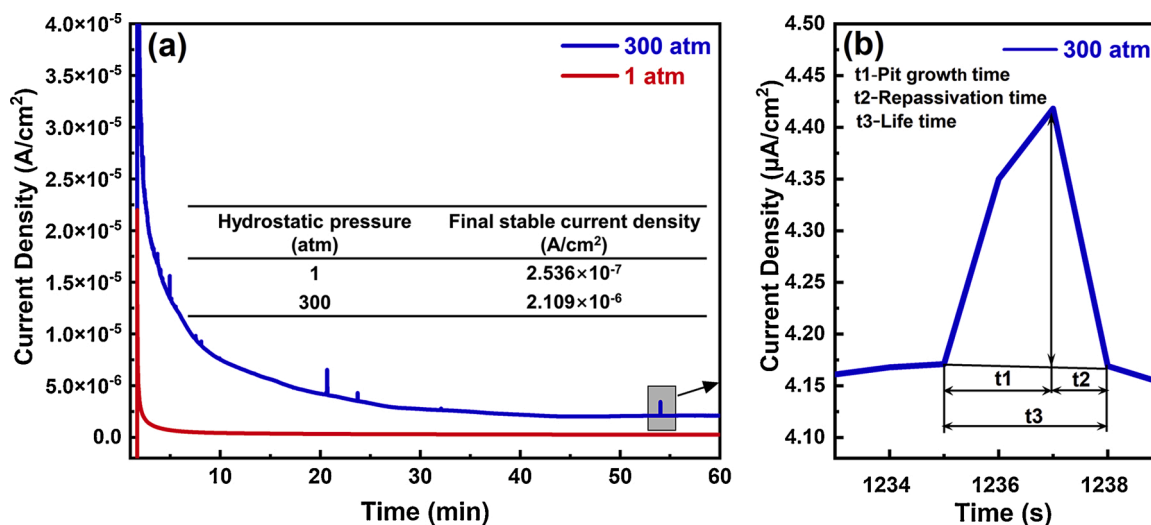

Fig. 7. Potentiostatic polarization curves of the Cr/GLC multilayered coating at the applied potential of 600 mV$_{Ag/AgCl}$ under both environment and the corresponding final stable current density (a) and typical shape of enlarged current transient (b).
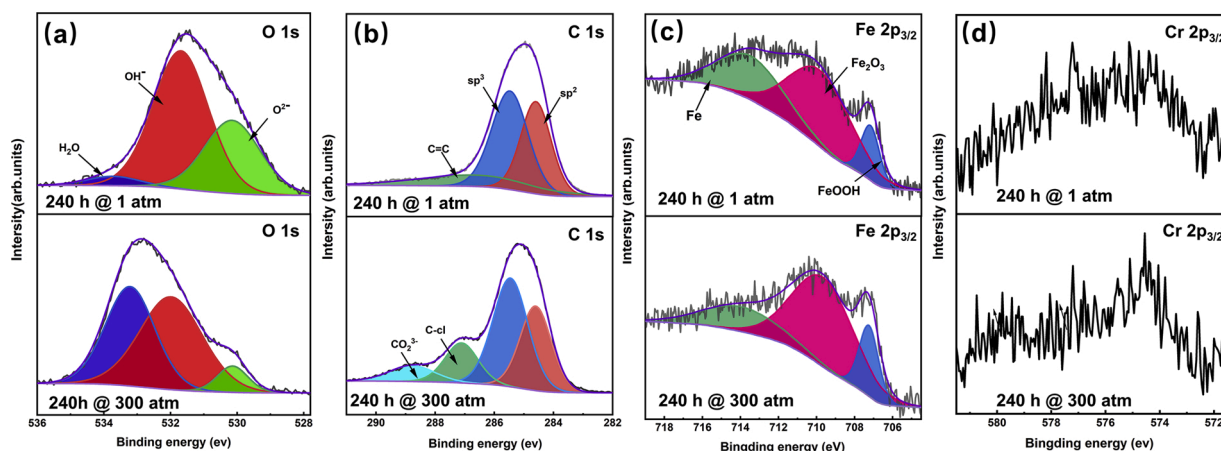
Fig. 8. XPS spectra of (a) O 1s, (b) C 1s, (c) Cr 2p$_{3/2}$ and (d) Fe 2p$_{3/2}$ of for the Cr/GLC multilayered coating after the immersion tests 240 h under both environments.

coating (shown in Fig. 2) presents the characteristic with different types of growth defects. The cross-sectional morphology of the coating shown in Fig. 3 proves that the periodic multilayered structure can prevent the pinholes from the surface extending to the substrate, but the nodular-like defect and penetrating defect cannot be sealed effectively [34–37]. Therefore, the plausible failure mechanisms for the amorphous carbon coating under hydrostatic pressure should be considered from the relationship between the hydrostatic pressure promoted corrosion process and the evolution of growth defects.

4.1. The influence of the hydrostatic pressure on the corrosion process

4.1.1. EIS analysis

In-situ EIS tests depicted in Figs. 4 and 5 provide an abundance of information regarding the corrosion process taking place at the coating surface and interface between substrate and coating. The experimental data are fitted with corresponding equivalent electrical circuits to understand the corrosion process in detail. To create a better fitting accuracy of the EIS data, the constant phase element (CPE) is applied to present the non-ideal electrical behavior of the coating, which is, as it is considered, caused by the non-homogeneous nature of the coating surface [10]. Furthermore, the diffusion behavior of reactive species through the defects is critical and always exists in the electrochemical corrosion process taking place at the such coatings deposited by PVD [17]. Thus, the Warburg impedance (*W*), the diffusion element usually used to model the semi-infinite diffusion behavior at the low frequency region, is introduced into the models shown in Fig. 9 to describe the diffusion process of corrosive species through the growth defects [38].

For the EIS data collected at 1 atm (Fig. 4), the impedance spectra show a perfect stable feature as a function of immersion time. Fig. 2(b)

shows that the bottom of penetrating defects still fills with imperfect coatings, but the defect which totally exposes the substrate cannot be ignored. Because the 316 L stainless steel is a relative passivate substrate, the dense and high dielectric constant passive film would form at the substrate-exposed sites [39]. Therefore, the almost unchanged impedance modulus (Fig. 4b) at 1 atm indicates that the Cr/GLC multilayered coating still maintains a stable protective performance with a relatively high corrosion resistance. The phase angle plot Fig. 4(b) shows the presence of an asymmetry, which suggests the presence of partially overlapped two time constants. For the Cr/GLC multilayered coating, the time constant at high frequency region may be related to the rapid charging/discharging process occurring at the coating/electrolyte interface, while the time constant at low frequency region to the slower process occurring at the substrate/coating interface [40]. Consequently, such an EIS characteristic can be approximately described by the model A (Fig. 9(a)). In the model A, R$_s$ presents the solution resistance, parallel-connected elements (CPE$_{(c+o)}$, R$_p$) are the total capacitance of the substrate/coating system and the pore resistance, where the subscript (c+o) stands for the Cr/GLC multilayered coating and the substrate passive film forms in the bottom of the penetrating defects.

As for the EIS results obtained at 300 atm, a gradual decrease of capacitive loop is clearly shown in Fig. 5(a), indicating a hydrostatic pressure-promoted corrosion process. The phase angle plot (Fig. 5(b)–(c)) clearly presents different stages with the increasing of the immersion time. At the initial immersion stage (in the first 2 h), the phase angle plot displays the same feature compared with that at 1 atm. That is, there are still two time constants at this stage. Consequently, model A is still rational to fit the EIS data at this initial stage. As immersion time increases, the partially overlapped two time constants can be distinguished gradually, one at high frequency (about 10^3 Hz) and another at
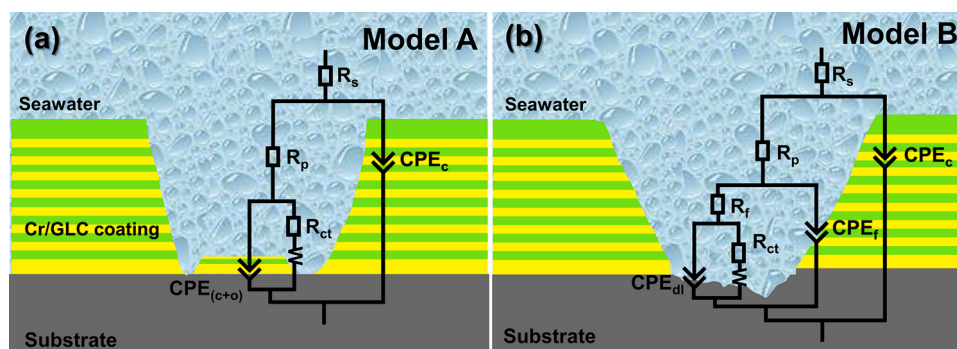

Fig. 9. Equivalent electrical circuits for fitting the EIS data of the Cr/GLC multilayered coating under both hydrostatic pressures. (a) for the model A which presents the coating at 1 atm and the initial stage of coating at 300 atm, (b) for the model B which present the coating at 300 atm in late stage of the immersion test.

low frequency (about 10 Hz). The high frequency phase angle peak at a lower phase angle region, reflecting the gradually enhanced non-ideal capacitive behavior at the coating/electrolyte interface. The gradually deviation from a near capacitive behavior of the double layer at the interface may be ascribed to the improved surface adsorption phenomenon, which is consist with the results of XPS in Fig. 8. While the presence of the second time constant at low frequency region can be explained with the permeation process of seawater through the growth defects, indicating the corrosion reaction starts at this stage. Therefore, model A is still suitable to fit the EIS data at this initial stage. As immersion time increases to more than 12 h, the phase angle at low frequency region decreases obviously and the position of the low frequency time constant shifts toward higher frequency region. These features indicate that the serious corrosion reaction has occurred at the growth defects. Further, according to the multilayered structure of the Cr/GLC coating, it should be noticed that the corrosion reaction does not only relate to the exposed substrate in the bottom of defects, but also to the exposed Cr buffer layers in the side wall of the penetrating defects. Consequently, a new model B (Fig. 9(b)) is introduced to fit the EIS data obtained after 12 h immersion test. In the model B, the CPE_c, CPE_f and CPE_{dll} are the constant phase elements presenting the non-ideal capacitance of the coating, the oxide film of the Cr buffer layer and the substrate double layer, respectively. The R_s, R_{ox} and R_{ct} indicate the seawater solution resistance, oxide layer resistance of Cr layers and charge transfer resistance, respectively. Here, the diffusional impedance W still exists during the EIS testing to describe the diffusion process of corrosive products through the penetrating defects. The fitting result of EIS spectra under 1 atm and 300 atm are listed in Tables S1 and S2, respectively.

4.1.2. The evolution of the coating corrosion resistance

The corresponding fitting results under both hydrostatic pressures fitted with the above equivalent electrical circuits are plotted as a function of immersion time in Fig. 10. Fig. 10(a) shows the corrosion potential (E_{corr}) curves. The curves present completely different tendencies during the immersion tests. The E_{corr} at 1 atm gradually increase and then attains a steady state about 0.2 V. Nevertheless, the E_{corr} at 300 atm shows typically two distinct regions with a dramatic potential decrease down to the minimum value and then reach a stationary value (about -0.7 $V_{Ag/AgCl}$). The significant decrease of E_{corr} values can be explained as the degradation of the air-formed passive film and electrochemical corrosion of Cr buffer layers in the penetrating defects. XPS results confirm that absorption of anion, such as Cl^-, occurred during the immersion test, which is a critical factor to the E_{corr} and also reported in the references [41–43]. Therefore, the rapid decrease of E_{corr} values at the first about 30 h stage is caused by the dramatic diffusion of seawater through the defects. And then the stable low-potential is caused by the enhanced anode reaction process due to the increased metal dissolution phenomenon. Generally, the protective properties of the coating can be presupposed from the charge-transfer resistance (R_{ct}), the higher value of R_{ct} means the greater corrosion resistance and slower corrosion reaction process [44–46]. The R_{ct} under both hydrostatic pressures presents plotted in Fig. 10(b). The curves show the trend of rapid decline firstly and then gradually decrease. But more significantly, the rapid
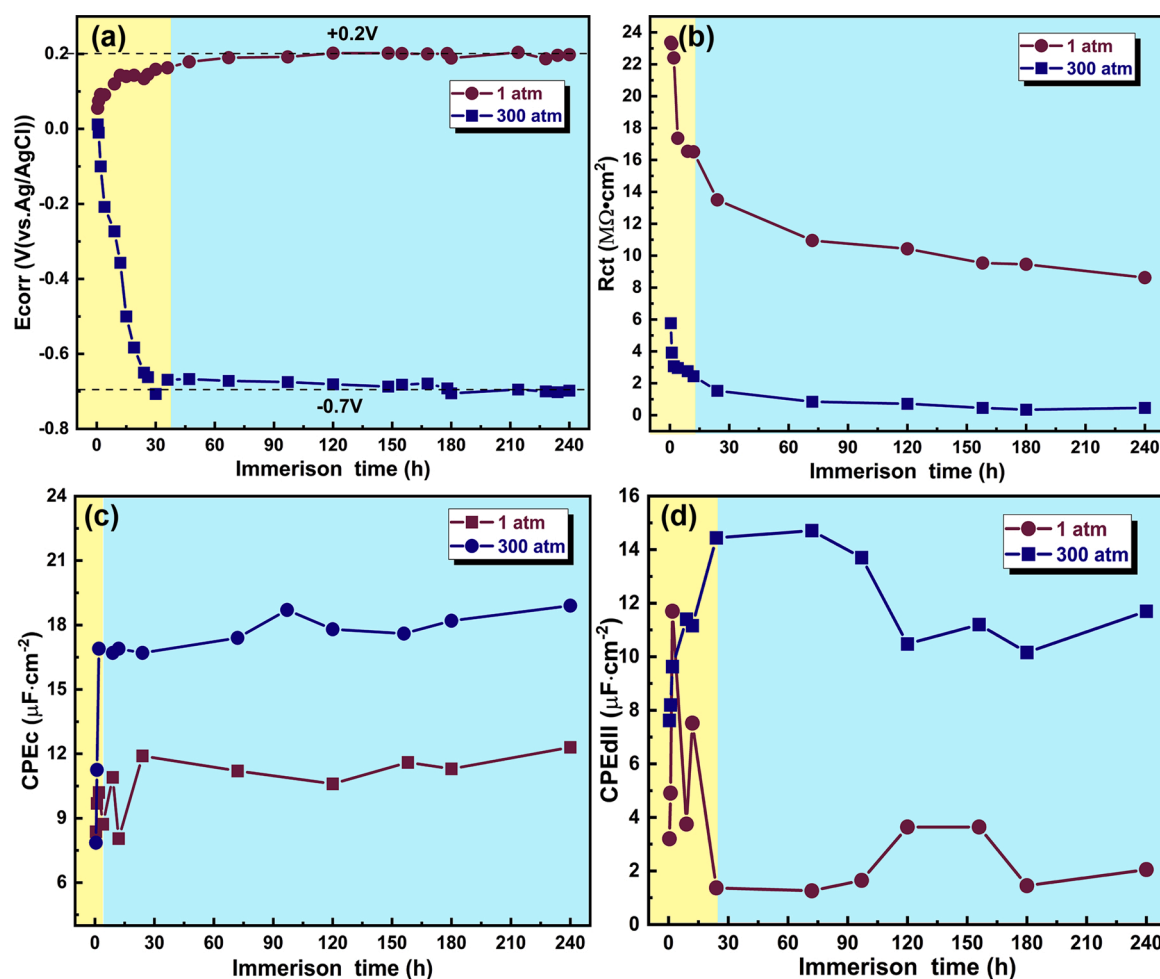

Fig. 10. Fitting results of the experimental EIS results as a function of immersion time under both hydrostatic pressures. (a) the corrosion potential E_{corr}, (b) the charge-transfer resistance R_{ct}, (c) the coating capacitance CPE_c, (d) the double layer capacitance CPE_{dll}.

reduction is found initially at 4 h at 300 atm. After the immersion tests, R_{ct} dropped from 5.77 MΩ cm^{-2} to 0.34 MΩ cm^{-2} at 300 atm, while it only decreased from 23.28 MΩ cm^{-2} to 8.62 MΩ cm^{-2} at 1 atm. The sharp drop of R_{ct} indicates that high hydrostatic pressure significantly deteriorated the protection of the coating. The change of R_{ct} reveals that the drastic corrosion reaction immediately occurs when the seawater reaches the substrate and then the persistent corrosion takes place with a relative high corrosion rate.

Fig. 10(c) presents the change of coating capacitance CPE_c during the immersion under both hydrostatic pressures. The CPE_c increases initially and then seems to keep steady thereafter in the vicinity of 18 μF cm^{-2} and 12 μF cm^{-2} at 1 atm and 300 atm, respectively. The higher CPE_c indicates that the hydrostatic pressure accelerates the corrosion process during the immersion test. The coating capacitance CPE_c is determined by the composition and microstructure of the coating materials [40,46], according to

$$CPE_c = \gamma \varepsilon_0 \varepsilon_c (1-P) A_c / d_c \tag{1}$$

where γ is the surface roughness factor, ε_0 is the permittivity of free space equal to 8.845×10^{-12} F/m, ε_c is the dielectric constant of the coating, P is the porosity of the coating, A_c is the exposed coating area in the test, d_c is the coating thickness equal to 1 μm. Assuming the coating is inert enough in the artificial seawater, it can be reasonably speculated that the surface γ and d_c maintain constant in the test. Similarly, the ε_c remains stable because the identical coating is adopted in the immersion test. Consequently, the coating capacitance CPE_c is determined by the coating porosity P and the exposed coating area A_c. Based on the analysis results of cyclic poloarization and potentiostatic tests, it can be readily interpreted that more and more growth defects are gradually revealed due to the promoted penetration of seawater at 300 atm. Therefore, it is reasonable to deduce that the coating porosity P increases under high hydrostatic pressure. By far, indeed, the increased value of CPE_c under hydrostatic pressure is determined by the coating area A_c. However, the exposed coating area A_c changes with the immersion time in two ways. On the one hand, because more growth defects evolute into active corrosion sites, A_c decreases. On the other hand, A_c also increases due to the revealed walls at the growth defects. The higher value of CPE_c portends the larger exposed coating area A_c, indicating that the increase in wall area is predominant under high hydrostatic pressure.

The double layer capacitance CPE_{dll}, as an indirect measure for the degree of substrate corrosion reaction, is plotted as a function of immersion time in Fig. 10(d). Obviously, the CPE_{dll} value at 300 atm is higher than that at 1 atm. Because the stainless steel is the conductive, the double layer capacitance is mainly determined by the capacitance of passive film [47]. Here, the double layer capacitance CPE_{dll} can be defined according to the following:

$$CPE_{dll} = \gamma \varepsilon_0 \varepsilon_{dll} A_s P / d_p \tag{2}$$

where the ε_{dll} is the dielectric constant of the passive film on the substrate, A_s is the exposed substrate area, d_p is the thickness of the passive film. Other parameters in Eq. (2) have the identical definition with Eq. (1). Previous studies indicated that the hydrostatic pressure would cause an inhomogeneity in thickness or even thickened passive film of the 316 L stainless steel substrate [48]. Therefore, the higher values of CPE_{dll} imply the larger reaction area of substrate at 300 atm. That is, the sharp drop of CPE_{dll} can be attributed to the severe substrate corrosion at the penetrating defects, as well as the more corrosion sites formed at 300 atm.

4.2. The evolution of growth defects under both hydrostatic pressures

Above EIS analysis has shown a quite different corrosion process under both hydrostatic pressures. The fitted electrochemical parameters at 300 atm change significantly at the initial stage and then reach a steady state, suggesting that the hydrostatic pressure promoted

corrosion process involves the process of fast diffusion of seawater and persistence electrochemical reaction on the substrate. In order to clarify the effect of hydrostatic pressure, the evolution of growth defects after the immersion under both hydrostatic pressures is analyzed in detail by means of SEM & FIB.

4.2.1. The evolution of the nodule-like defect

Fig. 11 is the surface and cross-sectional morphologies and corresponding EDS mapping results of nodular-like defect after immersion at 300 atm. The surface morphology of this kind of defect is covered with lots of ball-like particles (Fig. 11(a)) and looks uneven. But the corresponding EDS mapping (Fig. 11(b)) results indicate that the structure of Cr/GLC multilayered coating remains protective after the immersion test. The cross-sectional morphologies (Fig. 11(c)) provide clear images, where the Cr/GLC multilayered coating presents wave but still complete with a periodic multilayer structure. The corresponding EDS mapping (Fig. 11(d)) shows that the Cr/GLC multilayered coating is deposited on the remained inclusions which probably is the oxides of aluminum. Based on the above analysis, it can be identified that the nodular-like defect forms on the metallurgical inclusions. Because it still has a completed periodic multilayered structure, and possesses outstanding corrosion protection performance at 300 atm. Thus, the nodule-like defect is not the cause of the serious corrosion reaction under high hydrostatic pressure environment

4.2.2. The evolution of the penetrating defect

The corrosion morphology of penetrating defect after immersion at 1 atm is shown in Fig. 12. The formation mechanism can be illustrated as the adsorption and drop of impurities on the substrate surface during the deposition process [35]. Obviously, the fillers are still in the bottom of the defect (Fig. 12(a)). The corresponding EDS mapping results prove that the oxygen element mainly concentrates on the edge of the defect. The cross-sectional morphology (Fig. 12(c)) presents the complete profile of the substrate in the bottom of the defect. Detailed view in Fig. 12 (d) further proves a clear bulge on the substrate, which causes the folding formation of Cr/GLC multilayered coating during the rotation deposition process. Careful inspection shows that the edge of the defect presents sloping, which leads to the alternative exposure of Cr buffer layers and GLC layers. Evidently, the corrosion reaction mainly occurs along the edge of the defect where the Cr buffer layer is exposed. These findings indicate that the penetrating defect is still with the protectiveness performance during the immersion test under the atmospheric pressure and it is in a good agreement with the analysis results of EIS.

For a comparison, the structure of the penetrating defect after the immersion at 300 atm changes seriously (Fig. 13). Incomplete fillers do not exist on the bottom of the defect anymore (Fig. 13(a)). The stepped edge exposes the Cr buffer and inner GLC layer alternately. EDS mapping results (Fig. 13(b)) prove that the distribution of the chromium and oxygen elements concentrate on the whole edge of the defect, which indicates that the exposed Cr buffer layers are corroded seriously. The XPS result also proves that the oxidation of the Cr is more severe at 300 atm. The widely exposed GLC layers at the edge of multilayered confirm that the increased coating capacitance CPE_c in Fig. 11(c) is caused by the revealed side wall area on the edge of the penetrating defects. Because the potential difference exists in the Cr layers and GLC layers, the Cr buffer layers would corrode due to the galvanic corrosion [49]. The oxidation of Cr at the edge of the defect proves that the corrosion reaction occurs at the Cr buffer layers. Meanwhile, tensile stress around the localized corrosion sites induced by the hydrostatic pressure generates a shearing force around the edge of penetrating defects, which might destroy the structure of the defect as well [50]. The cross-sectional morphology, shown in Fig. 13(d), directly exhibits that serious corrosion reaction both occurred on the edge and bottom of the defect. Enlarged drawing shows in clarity that the defect bottom profile is far below to the substrate profile, and both at the Cr buffer layers and GLC layers spalls slightly. It is clearly indicated that the corrosion reaction is significantly
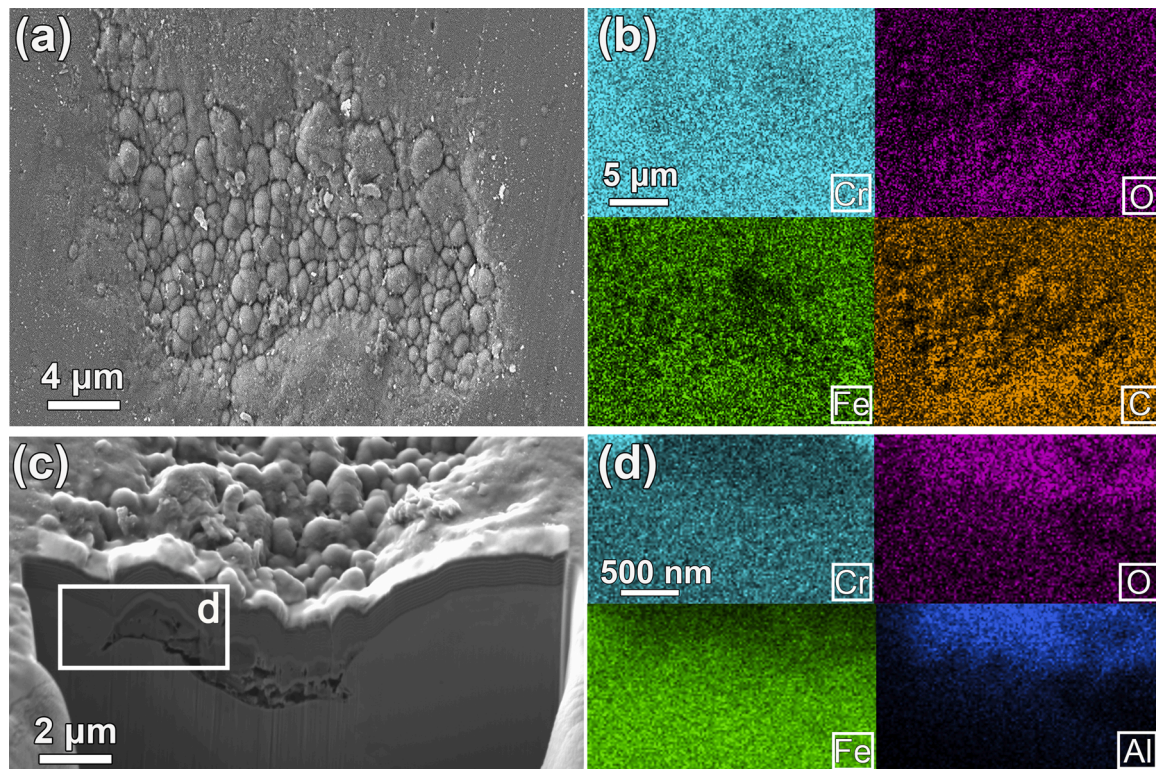
Fig. 11. The evolution of the nodule-like defect after the immersion test under high hydrostatic pressure. (a) surface morphology of the defect and (b) its corresponding EDS mapping results. (c) The cross-sectional image of the defect and (d) its EDS mapping results detected in the selected area in (c).
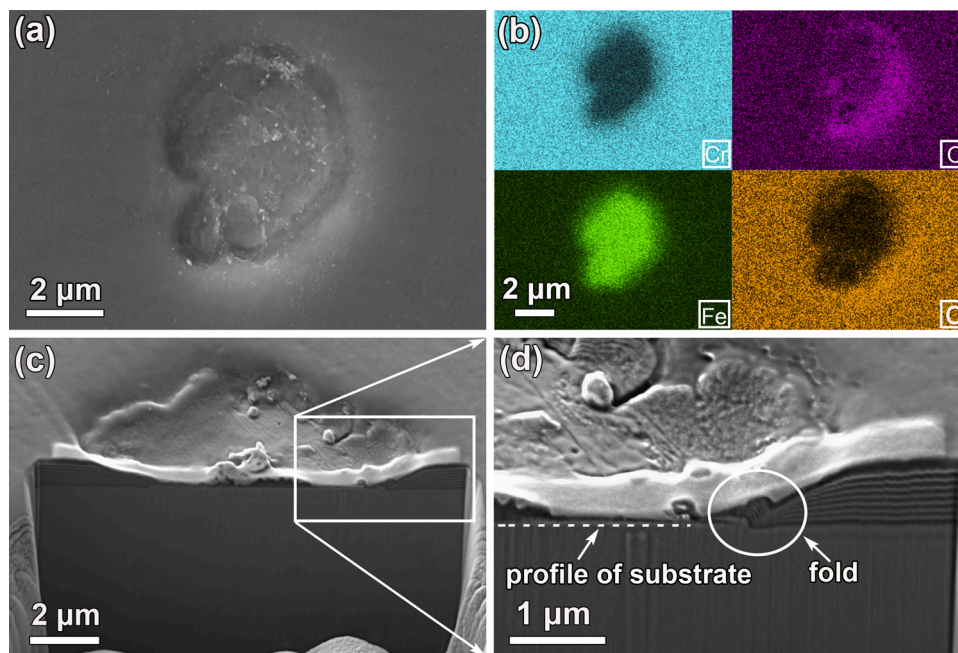

Fig. 12. The surface and cross-sectional morphologies of the through-thickness defect after immersion test 240 h under atmospheric pressure. (a) surface morphology of the defect; (b) The corresponding EDS mapping results of the defect; (c) cross-sectional image of the defect and (d) its local enlarged drawing.

promoted and the defect's structure is destroyed under the high hydrostatic pressure.

4.3. Failure mechanism

The failure behavior of the Cr/GLC multilayered coating under high

hydrostatic pressure has been demonstrated in Fig. 14, which has been illustrated well from the results discussed above. Nodular-like defects forms on the substrate inclusions and has a complete multilayered structure. Penetrating defects belong to the open type which allow the corrosive media diffusion through them. Under the high hydrostatic pressure, the corrosive media diffusion process through the penetrating
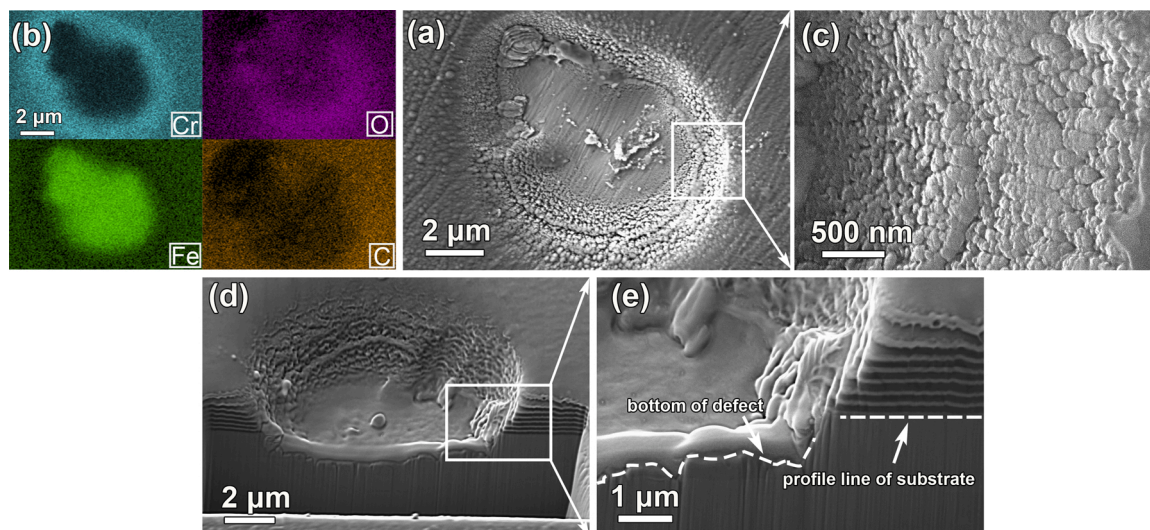
Fig. 13. The surface and the cross-sectional morphologies of the through-thickness defect after the immersion test 240 h under high hydrostatic pressure. (a) surface morphology of the defect and (b) its margin enlarged image; (c) corresponding EDS mapping results of the defect; (d) the cross-sectional image of the defect and (e) its local enlarged drawing.
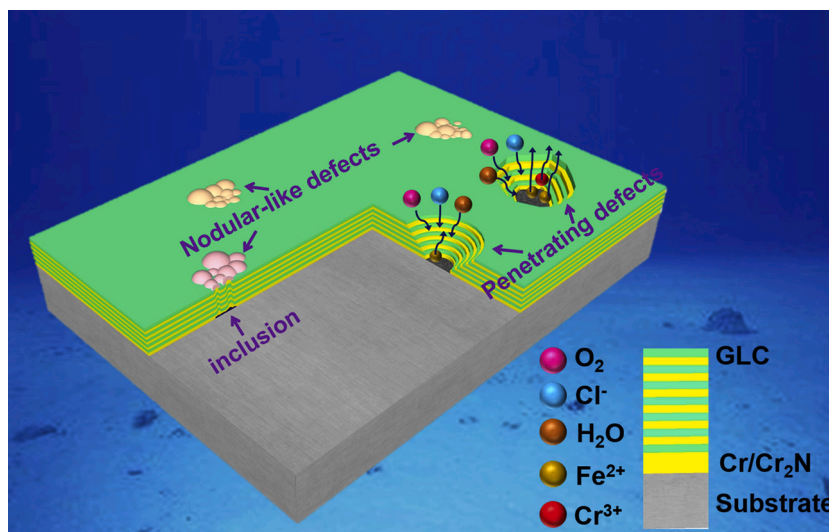

Fig. 14. Schematic cross-sections of failure process for the Cr/GLC multilayered coating under high hydrostatic pressure environment.

defect is greatly enhanced. As a result, lots of seawater reach the bottom of the defects rapidly and the corrosion reaction starts. With the extension of immersion time, the substrate at bottom of the penetrating defect corroded seriously. The galvanic corrosion between the Cr and GLC layers combined with the shearing force induced by the high hydrostatic pressure would also destroy the structure of the penetrating defects. Thus, it is obvious that the severe localized corrosion induced by the penetrating defects is responsible for the Cr/GLC multilayered coating degradation under higher hydrostatic pressure.

5. Conclusions

This work systematically investigates the corrosion behavior and the evolution of growth defects of the Cr/GLC multilayered coating at 1 atm and 300 atm. The corrosion resistance of the coating is almost unchanged after the immersion test at 1 atm, suggesting that the Cr/GLC multilayered coating is promising for the application in atmospheric pressure environment. However, the high hydrostatic pressure deteriorated the corrosion resistance of the coating severely. The

electrochemical tests and corrosion morphologies results prove that the high hydrostatic pressure promotes the diffusion process of seawater through the penetrating defects and accelerates the exposure of the substrate. Persistent corrosion reaction occurs at the bottom of the defects, as well as the destroyed structure of the penetrating defect during the immersion. As a result, a poor localized corrosion resistance of the Cr/GLC multilayered coating is presented under high hydrostatic pressure. This study sheds light on the deep understanding of corrosion process and growth defect evolution of the Cr/GLC multilayered coating under both hydrostatic pressures, which will be helpful for providing a basis upon which rational design of novel carbon-based coating can be proceeded.

Author contributions

Yingrui Liu: Conceptualization, Methodology Investigation, Validation and Writing-Original, **Hong Du:** Investigation, **Xiao Zuo:** Formal analysis, **Peng Guo:** Visualization, **Li Liu:** Methodology, **Kwang-Ryeol Lee:** Methodology, Visualization, **Aiying Wang:** Writing - Review &

Editing, Funding acquisition, Supervision, **Peiling Ke:** Writing - Review & Editing, Supervision, Funding acquisition.

Data availability statement

The data used to support the findings of this study are available from the corresponding author upon request.

Declaration of Competing Interest

The authors report no declarations of interest.

Acknowledgments

Appendix A. Supplementary data

Supplementary material related to this article can be found, in the online version, at doi:https://doi.org/10.1016/j.corsci.2021.109528.

References

[1] M. Schumacher, Sea Water Corrosion Handbook, Noye Data, New Jersey, 1979.

[2] P. Traverso, E. Canepa, A review of studies on corrosion of metals and alloys in deep-sea environment, Ocean. Eng. 87 (2014) 10–15, https://doi.org/10.1016/j.oceaneng.2014.05.003.

[3] A.M. Beccaria, P. Fiordiponti, G. Mattogno, The effect of hydrostatic pressure on the corrosion of nickel in slightly alkaline solutions containing Cl-ions, Corro. Sci. 29 (1989), https://doi.org/10.1016/0010-938X(89)90095-4, 403-&.

[4] A.M. Beccaria, G. Poggi, P. Castello, Influence of passive coating composition and sea water pressure on resistance to localized corrosion of some stainless steels in sea water, Br. Corros. J. 30 (1994) 283–287, https://doi.org/10.1179/000705995798113709.

[5] A.M. Beccaria, G. Poggi, Influence of hydrostatic pressure on pitting of aluminium in sea water, Br. Corros. J. 20 (2013) 183–186, https://doi.org/10.1179/000705985798272632.

[6] A.M. Beccaria, G. Poggi, D. Gingaud, P. Castello, Effect of hydrostatic pressure on passivating power of corrosion layers formed on 6061 T6 aluminum alloy in sea water, Br. Corros. J. 29 (1994) 65–69, https://doi.org/10.1179/000705994798267962.

[7] Z.X. Yang, B. Kan, J.X. Li, Y.J. Su, L.J. Qiao, Hydrostatic pressure effects on corrosion behavior of X70 pipeline steel in a simulated deep-sea environment, J. Electroanal. Chem. 822 (2018) 123–133, https://doi.org/10.1016/j.jelechem.2018.05.010.

[8] Y. Yang, T. Zhang, Y. Shao, G. Meng, F. Wang, Effect of hydrostatic pressure on the corrosion behavior of Ni–Cr–Mo–V high strength steel, Corros. Sci. 52 (2010) 2697–2706, https://doi.org/10.1016/j.corsci.2010.04.025.

[9] T. Zhang, Y. Yang, Y. Shao, G. Meng, F. Wang, A stochastic analysis of the effect of hydrostatic pressure on the pit corrosion of Fe–20Cr alloy, Electrochim. Acta 54 (2009) 3915–3922, https://doi.org/10.1016/j.electacta.2009.02.010.

[10] Y. Liu, J. Wang, L. Liu, Y. Li, F. Wang, Study of the failure mechanism of an epoxy coating system under high hydrostatic pressure, Corros. Sci. 74 (2013) 59–70, https://doi.org/10.1016/j.corsci.2013.04.012.

[11] W.L. Tian, F.D. Meng, L. Liu, Y. Li, F.H. Wang, Lifetime prediction for organic coating under alternating hydrostatic pressure by artificial neural network, Sci. Rep. 7 (2017), 40827, https://doi.org/10.1038/srep40827.

[12] L. Liu, Y. Cui, Y. Li, T. Zhang, F. Wang, Failure behavior of nano-SiO2 fillers epoxy coating under hydrostatic pressure, Electrochim. Acta 62 (2012) 42–50, https://doi.org/10.1016/j.electacta.2011.11.067.

[13] W.L. Tian, L. Liu, F.D. Meng, Y. Liu, Y. Li, F.H. Wang, The failure behavior of an epoxy glass flake coating/steel system under marine alternating hydrostatic pressure, Corros. Sci. 86 (2014) 81–92, https://doi.org/10.1016/j.corsci.2014.04.038.

[14] C. Zhang, Z.W. Zhang, Q. Chen, L. Liu, Effect of hydrostatic pressure on the corrosion behavior of HVOF-sprayed Fe-based amorphous coating, J. Alloys Compd. 758 (2018) 108–115, https://doi.org/10.1016/j.jallcom.2018.05.100.

[15] X. Guan, L. Wang, The tribological performances of multilayer graphite-like carbon (GLC) coatings sliding against polymers for mechanical seals in water environments, Tribo. Lett. 47 (2012) 67–78, https://doi.org/10.1007/s11249-012-9963-2.

[16] J. Robertson, Diamond-like amorphous carbon, Mater. Sci. Eng. R 37 (2002) 129–281, https://doi.org/10.1016/S0927-796X(02)00005-0.

[17] A.M.M. dos Santos, R.J.C. Batista, L.A.M. Martins, M. Ilha, M.Q. Vieira, D. R. Miquita, F.C.R. Guma, I.L. Muller, T.M. Manhabosco, Corrosion and cell viability studies of graphite-like hydrogenated amorphous carbon films deposited on bare and nitrided titanium alloy, Corros. Sci. 82 (2014) 297–303, https://doi.org/10.1016/j.corsci.2014.01.025.

[18] F. Yan, B. Jiang, W. Shao, J. Shi, Majorization of GLC properties by the introduction of silver nanowires as conductive framework for metal bipolar plates, Appl. Surf. Sci. 533 (2020), https://doi.org/10.1016/j.apsusc.2020.147493.

[19] S. Khamseh, E. Alibakhshi, B. Ramezanzadeh, M.G. Sari, A.K. Nezhad, Developing a graphite like carbon: niobium thin film on GTD-450 stainless steel substrate, Appl. Surf. Sci. 511 (2020), https://doi.org/10.1016/j.apsusc.2020.145613.

[20] R. Hauert, G. Thorwarth, U. Muller, M. Stiefel, C.V. Falub, K. Thorwarth, T. J. Joyce, Analysis of the in-vivo failure of the adhesive interlayer for a DLC coated articulating metatarsophalangeal joint, Diam. Relat. Mat. 25 (2012) 34–39, https://doi.org/10.1016/j.diamond.2012.02.001.

[21] M. Fenker, M. Balzer, H.A. Jehn, H. Kappl, J.J. Lee, K.H. Lee, H.S. Park, Improvement of the corrosion resistance of hard wear resistant coatings by intermediate plasma etching or multilayered structure, Surf. Coat. Technol. 150 (2002) 101–106, https://doi.org/10.1016/s0257-8972(01)01506-7.

[22] X.W. Li, L. Li, D. Zhang, A. Wang, Ab initio study of interfacial structure transformation of amorphous carbon catalyzed by Ti, Cr, and W transition layers, ACS Appl. Mater. Interf. 9 (2017) 41115–41119, https://doi.org/10.1021/acsami.7b12179.

[23] E. Härkönen, J. Kolev, B. Díaz, J. Swiatowska, V. Maurice, A. Seyeux, P. Marcus, M. Fenker, L. Toth, G. Radnoczi, et al., Sealing of hard CrN and DLC coatings with atomic layer deposition, ACS Appl. Mater. Interfaces 6 (2014) 1893–1901, https://doi.org/10.1021/am404906x.

[24] L. Li, P. Guo, L.-L. Liu, X. Li, P. Ke, A. Wang, Structural design of Cr/GLC films for high tribological performance in artificial seawater: Cr/GLC ratio and multilayer structure, J. Mater. Sci. Technol. 34 (2018) 1273–1280, https://doi.org/10.1016/j.jmst.2017.12.002.

[25] L. Li, L.L. Liu, X. Li, P. Guo, P. Ke, A. Wang, Enhanced tribocorrosion performance of Cr/GLC multilayered coating for marine protective application, ACS Appl. Mater. Interf 10 (2018) 13187–13198, https://doi.org/10.1021/acsami.8b00628.

[26] J. Qiu, Y. Zou, G. Yu, H. Liu, Y. Jia, Z. Li, P. Huai, X. Zhou, H. Xu, Compatibility of container materials with Cr in molten FLiNaK salt, J. Fluorine Chem. 168 (2014) 69–74, https://doi.org/10.1016/j.jfluchem.2014.09.010.

[27] ASTMD1141-1198, Standard Practice for the Preparation of Substitute Ocean Water, United States, 2008.

[28] S.C. Dexter, C. Culberson, Global variability of natural sea water, Mater. Perform. 19 (1980) 16–28.

[29] G.S. Frankel, Pitting corrosion of metals - a review of the critical factors, J. Electrochem. Soc. 145 (1998) 2186–2198, https://doi.org/10.1149/1.1838615.

[30] G. Burstein, P. Pistorius, S. Mattin, The nucleation and growth of corrosion pits on stainless steel, Corros. Sci. 35 (1–4) (1993) 57–62, https://doi.org/10.1016/0010-938X(93)90133-2.

[31] K. Chi, Z. Zhang, Q. Lv, C. Xie, J. Xiao, F. Xiao, S. Wang, Well-ordered oxygen deficient CoMoO4 and Fe2O3 nanoplate arrays on 3D graphene foam: toward flexible asymmetric supercapacitors with enhanced capacitive properties, ACS Appl. Mater. Interfaces 9 (2017) 6044–6053, https://doi.org/10.1021/acsami.6b14810.

[32] G. Chen, L. Xue, J. Wang, Z. Tang, X. Li, H. Dong, Investigation of surface modifications for combating the molten aluminum corrosion of AISI H13 steel, Corros. Sci. 174 (2020) 108836, https://doi.org/10.1016/j.corsci.2020.108836.

[33] S. Viswanathan, L. Mohan, P. Bera, V.P. Kumar, H.C. Barshilia, C. Anandan, Corrosion and wear behaviors of Cr-doped diamond-like carbon coatings, J. Mater. Eng. Perform. 26 (2017) 3633–3647, https://doi.org/10.1007/s11665-017-2783-7.

[34] S.H. Ahn, J.H. Lee, J.G. Kim, J.G. Han, Localized corrosion mechanisms of the multilayered coatings related to growth defects, Surf. Coat. Technol. 177–178 (2004) 638–644, https://doi.org/10.1016/s0257-8972(03)00939-3.

[35] D.M. Mattox, Surface effects on the growth, adhesion and properties of reactively deposited hard coatings, Surf. Coat. Technol. 81 (1996) 8–16, https://doi.org/10.1016/0257-8972(95)02652-5.

[36] A.M. Marques dos Santos, R.J. Campos Batista, L.A. Meira Martins, M. Ilha, M. Q. Vieira, D.R. Miquita, F.C. Rodrigues Guma, I.L. Mueller, T.M. Manhabosco, Corrosion and cell viability studies of graphite-like hydrogenated amorphous carbon films deposited on bare and nitrided titanium alloy, Corros. Sci. 82 (2014) 297–303, https://doi.org/10.1016/j.corsci.2014.01.025.

[37] N.W. Khun, E. Liu, X.T. Zeng, Corrosion behavior of nitrogen doped diamond-like carbon thin films in NaCl solutions, Corros. Sci. 51 (2009) 2158–2164, https://doi.org/10.1016/j.corsci.2009.05.050.

[38] C. Liu, Q. Bi, A. Leyland, A. Matthews, An electrochemical impedance spectroscopy study of the corrosion behaviour of PVD coated steels in 0.5 N NaCl aqueous solution: Part I. Establishment of equivalent circuits for EIS data modelling, Corros. Sci. 45 (2003) 1243–1256, https://doi.org/10.1016/S0010-938X(02)00213-5.

[39] J. Dai, H. Feng, H.-B. Li, Z.-H. Jiang, H. Li, S.-C. Zhang, P. Zhou, T. Zhang, Nitrogen significantly enhances corrosion resistance of 316L stainless steel in thiosulfate-chloride solution, Corros. Sci. 174 (2020) 108792, https://doi.org/10.1016/j.corsci.2020.108792.

[40] C. Liu, Q. Bi, A. Leyland, A. Matthews, An electrochemical impedance spectroscopy study of the corrosion behaviour of PVD coated steels in 0.5 N NaCl aqueous solution: part II.: EIS interpretation of corrosion behaviour, Corros. Sci. 45 (2003) 1257–1273, https://doi.org/10.1016/S0010-938X(02)00214-7.

[41] R. Liu, Y. Cui, L. Liu, F. Wang, Study on the mechanism of hydrostatic pressure promoting electrochemical corrosion of pure iron in 3.5% NaCl solution, Acta Mater. 203 (2021), https://doi.org/10.1016/j.actamat.2020.11.009.

[42] R. Liu, Y. Cui, L. Liu, B. Zhang, F. Wang, A primary study of the effect of hydrostatic pressure on stress corrosion cracking of Ti-6Al-4V alloy in 3.5% NaCl solution, Corros. Sci. 165 (2020), https://doi.org/10.1016/j.corsci.2019.108402.

[43] M. Mahdavian, A.R. Tehrani-Bagha, E. Alibakhshi, S. Ashhari, M.J. Palimi, S. Farashi, S. Javadian, F. Ektefa, Corrosion of mild steel in hydrochloric acid solution in the presence of two cationic gemini surfactants with and without hydroxyl substituted spacers, Corros. Sci. 137 (2018) 62–75, https://doi.org/10.1016/j.corsci.2018.03.034.

[44] S. Khamseh, E. Alibakhshi, B. Ramezanzadeh, J.-S. Lecomte, P. Laheurte, X. Noirefalize, F. Laoutid, H. Vahabi, Tailoring hardness and electrochemical performance of TC4 coated Cu/a-C thin coating with introducing second metal Zr, Corros. Sci. 172 (2020) 108713, https://doi.org/10.1016/j.corsci.2020.108713.

[45] C.O.A. Olsson, D. Landolt, Passive films on stainless steels—chemistry, structure and growth, Electrochim. Acta 48 (2003) 1093–1104, https://doi.org/10.1016/S0013-4686(02)00841-1.

[46] F. Mansfeld, C.H.J.C. Tsai, Determination of coating deterioration with EIS: I. Basic relationships, Corrosion 47 (1991) 958–963, https://doi.org/10.5006/1.3585209.

[47] S. Rudenja, J. Pan, I.O. Wallinder, C. Leygraf, P. Kulu, Passivation and anodic oxidation of duplex TiN coating on stainless steel, J. Electrochem. Soc. 146 (11) (1999) 4082–4086, https://doi.org/10.1149/1.1392595.

[48] C. Zhang, Z.-W. Zhang, L. Liu, Degradation in pitting resistance of 316L stainless steel under hydrostatic pressure, Electrochim. Acta 210 (2016) 401–406, https://doi.org/10.1016/j.electacta.2016.05.169.

[49] J. Qiu, A. Wu, Y. Li, Y. Xu, R. Scarlat, D.D. Macdonald, Galvanic corrosion of Type 316L stainless steel and Graphite in molten fluoride salt, Corros. Sci. 170 (2020), https://doi.org/10.1016/j.corsci.2020.108677.

[50] Y. Yang, T. Zhang, Y. Shao, G. Meng, F. Wang, New understanding of the effect of hydrostatic pressure on the corrosion of Ni–Cr–Mo–V high strength steel, Corros. Sci. 73 (2013) 250–261, https://doi.org/10.1016/j.corsci.2013.04.013.